https://doi.org/10.5194/egusphere-2026-1406
Preprint. Discussion started: 31 March 2026

# A Joint Space-Time Probabilistic Model for Agricultural Droughts, Hydrological Droughts and Fire Weather in France

Benjamin Renard[1], Renaud Barbero[1], Issa Goukouni[1], Jean-Philippe Vidal[2], Louise Mimeau[2], Carina Furusho-Percot[3], Iñaki García de Cortázar-Atauri[3], Maël Aubry[3], Thomas Opitz[4], and Denis Allard[4]

[1]INRAE, Aix Marseille University, UR RECOVER, Aix-En-Provence, France
[2]INRAE, UR RIVERLY, Lyon, France
[3]INRAE, US Agroclim, Avignon, France
[4]INRAE, Biostatistics and Spatial Processes (BioSP), Avignon, France

**Correspondence:** Benjamin Renard (benjamin.renard@inrae.fr)

**Abstract.** Agricultural droughts, hydrological droughts and wildfires have significant environmental and socioeconomic consequences. These hazards are physically linked because they share a number of forcings, and their space-time properties are important as impacts result from their spatial extent and duration, in addition to their intensity. This paper introduces a probabilistic model adapted to the description of multiple spatial hazards, based on the combination of simple ingredients: regressions to describe dependencies between hazards, principal component analysis to describe spatial dependence, and simple covariance functions to describe time dependence and residual spatial dependence. This results in a modular framework that decomposes a complex model into several simpler models. This model is then used to analyze the observed Soil Wetness Index, Fire Weather Index and river flows in France over the last six decades, and in particular to estimate the probability of occurrence of the remarkable 2022 summer event. Locally, the 2022 summer was extreme in terms of agricultural drought over a large part of the country, but was rather moderate in terms of hydrological drought and fire weather. However, the magnitude, spatial extent and duration of the event become extreme nearly everywhere when the three hazards are considered together. The underlying trends affecting all three hazards have more than doubled the probability of the event during the historical period, and future projections suggest that it might become common by the end of the century with global warming.

## 1 Introduction

In 2022, warm and dry conditions prevailed across the Northern Hemisphere, with Europe experiencing the most widespread simultaneous warm–dry compound event since 1950 (Meng et al., 2023). These conditions were linked across Western Europe to a persistent anticyclonic circulation pattern (Faranda et al., 2023), which for some regions led to the highest total water storage deficit observed since the start of satellite measurements in 2002 and to the most severe and widespread soil-moisture depletion over the past six decades (Bevacqua et al., 2024). Those particularly dry climate conditions took place against a backdrop of long-term warming, with Europe witnessing an annual temperature that was 2.3 °C above the pre-industrial level and its warmest summer on record (Copernicus Climate Change Service, 2023).

https://doi.org/10.5194/egusphere-2026-1406
Preprint. Discussion started: 31 March 2026

This drought led to multiple climate-related hazards. A technical report estimated the economic impact of the 2022 drought in France at approximately €5 billion (Commissariat général au développement durable, 2025), encompassing a range of direct effects, including structural damage, energy production, water resources, agricultural yields, and forest losses. For instance, reduced crop yields in 2022 led to an estimated €1.1 billion loss in production, and a record number of drought restriction orders were issued to curb water use. The river drying and the decline in reservoir levels significantly affected hydropower production, which is the second-largest source of electricity in France. At the same time, a total of 72,000 ha of vegetation burned across the country, including a large portion in the Southwest (Rodrigues et al., 2023) due to severe fire weather conditions amplified by anthropogenic climate change (Lanet et al., 2024). The extent of burned area caused a considerable biomass loss in the Atlantic pine forests (Vallet et al., 2023) and generated an estimated 441,000 tons of $CO_2$ emissions. Collectively, these hazards have posed significant challenges for drought risk management (Biella et al., 2025), as highlighted more recently during the summer of 2025 (Usman et al., 2025; Keeping et al., 2025), and are likely to remain a major concern in the light of future climate projections.

This raises the question of how rare the 2022 combined summer event in France actually was, and how rare similar events will be in the future? This type of framing is commonly used in attribution studies to assess the changing likelihood of an extreme weather event with time (e.g., Christidis et al. (2015)). However, this task is not always straightforward as the response may strongly vary depending on whether the hazards are analyzed individually or jointly, whether the focus is placed on their local intensity or their spatial extent, and depending on how the data is aggregated in space and time (Philip et al., 2020; Leach et al., 2020; Kirchmeier-Young et al., 2019; Angélil et al., 2018; Cattiaux and Ribes, 2018). These methodological choices may produce different estimates and different conclusions on how exceptional the 2022 episode truly was.

A substantial body of literature has already examined compound events in climate sciences, with approaches that can be broadly divided into two categories. A first group of studies focused on describing the properties of compound events from an empirical point of view, documenting how different hazards co-occur (Wang et al., 2012; Abatzoglou et al., 2020; Richardson et al., 2022; Deng et al., 2024). These studies typically provide insights into the physical mechanisms and spatiotemporal patterns underlying compound events, showing for instance, the increasing synchrony between heatwaves, drought, and fire-prone weather conditions. A second body of research has used probabilistic frameworks to quantify the likelihood of compound events and assess how rare these events are, and how they might change in a warming climate (Manning et al., 2019; Ridder et al., 2020; Squire et al., 2021; Jacquemin et al., 2026). For instance, Zscheischler et al. (2021) used nonparametric dependence modelling based on multivariate extreme-value theory to compare how wind and precipitation compounds are represented in both reanalyses and unconditioned climate model simulations. Copula-based methods have also been suggested for compound event attribution (Zscheischler and Lehner, 2022) to represent the dependence between variables and quantify the contribution of anthropogenic forcing to the probability of joint extremes.

Among previous studies, several have specifically focused on drought and fire-prone weather conditions to identify global hotspots (Ridder et al., 2020) or to evaluate the performance of climate model emulators in reproducing those compound events (Quilcaille et al., 2023). Other studies have shown that drought is often the primary precursor in cascading hazards, with drought and fire-prone weather situations representing the most recurrent compound events in Europe (Sutanto et al., 2020). Richardson et al. (2022) showed that burned area tends to be higher when periods of elevated fire-weather coincide with longer-term soil-moisture deficits, and that the frequency of such compound events has increased across large portions of the globe over recent decades. A case study of the 2019 Australian megafires provided additional evidence that both drought and fire-weather conditions reached unprecedented levels in the observational record with a 0.5 % annual probability of joint occurrences, collectively contributing to this extreme fire season (Squire et al., 2021).

Here, we develop a probabilistic framework that describes the time-varying joint distribution of several spatially indexed variables, to capture their dependence structure and how it might change under a warming climate. Second, we seek to evaluate whether a combination of simple tools – principal component analysis (PCA) for spatial dependence and regressions for inter-variable dependences – is sufficient to reproduce multivariate spatialized signals. We address these objectives through a national-scale case study in France, where the warming (about +1.66°C) lies above the global average (Ribes et al., 2022), with even stronger warming during the summer season. France encompasses several climate hotspots, including Mediterranean areas where heatwaves, drought, and fire-prone weather conditions have collectively increased in frequency and intensity over time (Cramer et al., 2018), which provides a particularly relevant context for investigating compound events. Finally, we illustrate how this model can be used by examining how exceptional the 2022 summer was in France (and how exceptional it will be in the future), viewed through the lens of agricultural drought, hydrological drought and fire-weather conditions.

## 2 Data

The data used in this study are illustrated in Figure 1 and described thereafter. Soil Wetness Index (SWI) data over the period 1959-2023 are provided by the SURFEX land surface scheme (Le Moigne et al., 2020) as driven by the SAFRAN near-surface meteorological reanalysis (Vidal et al., 2010a). SWI represents the total water content in the soil layer, normalized by the water content at field capacity and at wilting point (see Vidal et al., 2010b, for computation details). Original data, available at a daily resolution on a regular 8-km grid, are temporally averaged at a monthly time step and spatially averaged on a regular 0.25° longitude-latitude grid (using bilinear interpolation). The coarsening of the original spatial grid drastically reduces the memory requirement of the analysis, with limited impact on the results given the spatial smoothness of monthly SWI data. Note that SWI may take negative values (when the water content goes below the water content at wilting point), but this is extremely rare (less than 0.007% of the data). Negative values are replaced by a small positive value ($10^{-3}$) to enable the use of a log-transformation (see section 3.2).

Fire-weather conditions are represented using the commonly used Fire Weather Index (FWI) based on the method described by Van Wagner (1987). FWI data are derived from the SAFRAN reanalysis and are available over the period 1959-2023. FWI is a positive index, with large values corresponding to fire-prone conditions. FWI data are temporally and spatially averaged in the same way as SWI data.

Monthly streamflow (Q) data are provided by 580 hydrometric stations selected as part of the Explore2 project (Strohmenger et al., 2023) and gauging near-natural catchments. Unlike SWI and FWI data, the period of availability is station-specific (see

| Number | GCM | RCM | Starting Year |
|---|---|---|---|
| 1 | CNRM-CERFACS-CNRM-CM5 | CNRM-ALADIN63 | 1951 |
| 2 | CNRM-CERFACS-CNRM-CM5 | MOHC-HadREM3-GA7-05 | 1952 |
| 3 | ICHEC-EC-EARTH | KNMI-RACMO22E | 1951 |
| 4 | ICHEC-EC-EARTH | MOHC-HadREM3-GA7-05 | 1952 |
| 5 | ICHEC-EC-EARTH | SMHI-RCA4 | 1970 |
| 6 | IPSL-IPSL-CM5A-MR | DMI-HIRHAM5 | 1952 |
| 7 | IPSL-IPSL-CM5A-MR | SMHI-RCA4 | 1971 |
| 8 | MOHC-HadGEM2-ES | CLMcom-CCLM4-8-17 | 1951 |
| 9 | MOHC-HadGEM2-ES | CNRM-ALADIN63 | 1951 |
| 10 | MOHC-HadGEM2-ES | ICTP-RegCM4-6 | 1972 |
| 11 | MOHC-HadGEM2-ES | MOHC-HadREM3-GA7-05 | 1953 |
| 12 | MPI-M-MPI-ESM-LR | CLMcom-CCLM4-8-17 | 1951 |
| 13 | MPI-M-MPI-ESM-LR | ICTP-RegCM4-6 | 1971 |
| 14 | MPI-M-MPI-ESM-LR | MPI-CSC-REMO2009 | 1971 |
| 15 | NCC-NorESM1-M | DMI-HIRHAM5 | 1952 |
| 16 | NCC-NorESM1-M | GERICS-REMO2015 | 1951 |
| 17 | NCC-NorESM1-M | IPSL-WRF381P | 1952 |

**Table 1.** GCM-RCM combinations from the EURO-CORDEX experiment

Supplementary Figure S1). Moreover, the spatial support of Q (stations) differs from that of SWI and FWI (pixels). Spatial supports will be matched by averaging the SWI/FWI pixels contained within the catchment covered by each station.

Data at a specific location are used throughout this paper to illustrate results. More specifically, streamflow are taken from the station ‘The Tarn River at Bedoues‘, controlling a catchment of 189 $km^2$, and (SWI, FWI) values are taken at the nearest pixel. These data are shown in Figure 1 and will be consistently referred to as data from ‘the Tarn example pixel/station‘.

We will also use SWI projections derived from 17 Global Climate Model / Regional Climate Model (GCM/RCM) combinations (Table 1) from the CMIP5/EURO-CORDEX experiment (Jacob et al., 2014) under RCP8.5 scenario and bias-corrected with the ADAMONT method (Verfaillie et al., 2017). This projection dataset is described in detail by Robin et al. (2024) and Marson et al. (2024). The starting date of climate projections varies between the early 50s and the early 70s depending on the GCM/RCM combination, as specified in Table 1. SWI on the same 8 km regular grid is obtained using SURFEX forced by these climate projections under historical greenhouse gas conditions until 2005, and under the RCP8.5 emissions scenarios afterwards until 2100. All SWI projections are temporally averaged at a monthly time step and spatially averaged on the same regular 0.25° grid as before.

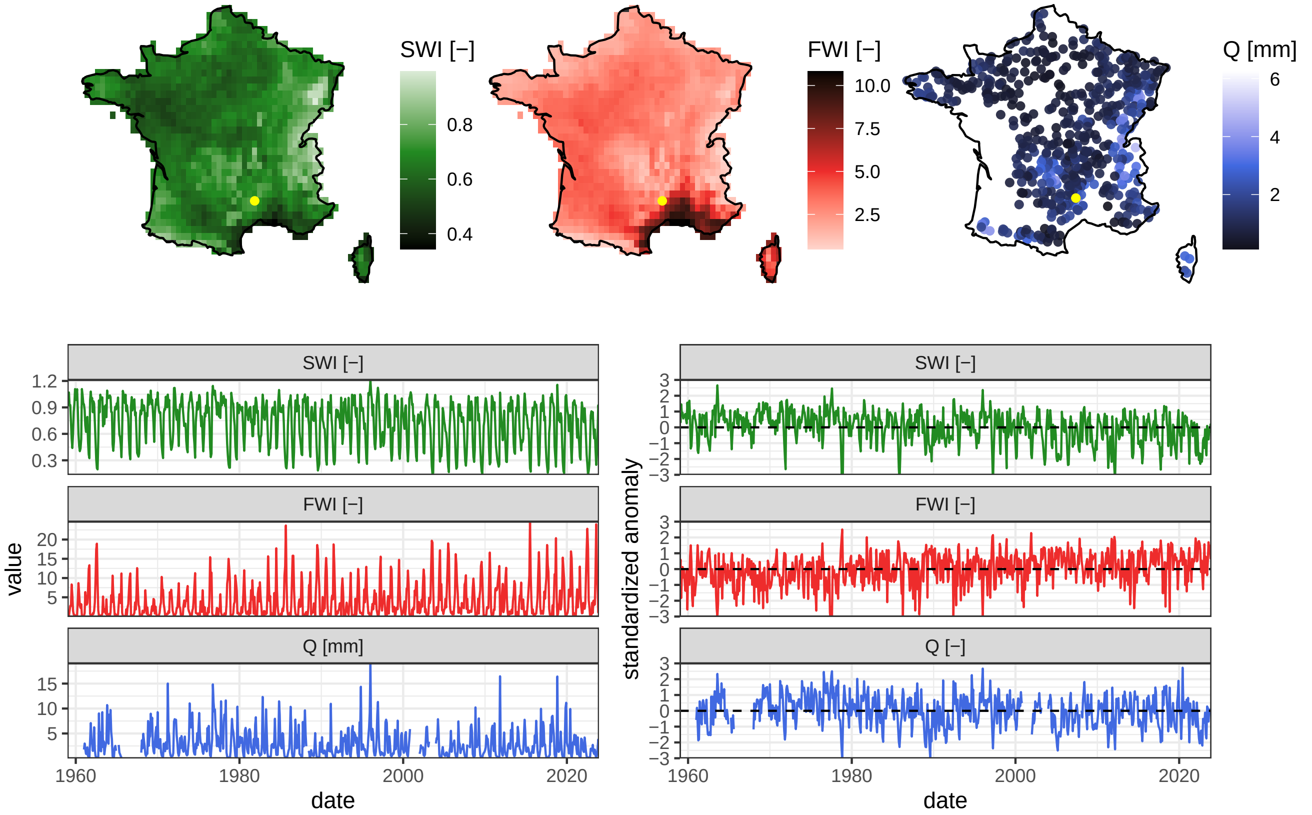

**Figure 1.** Data illustration. Top: maps of interannual average values. Bottom: example monthly time series (left) and corresponding standardized anomalies (right) for the hydrometric station 'The Tarn River at Bedoues' (Q) and the two nearest pixels (SWI, FWI), shown as yellow dots in the maps.

## 3 Methods

### 3.1 General Principle

The principle behind the proposed model is to postulate a causal graph that describes causal relations between the studied variables, and that should be able to explain the observed dependency between them. When the variables vary in space and time, an additional space-time model needs to be added at least for the variables sitting at the root of the graph (i.e. unforced variables). The resulting space-time dependencies and signals will propagate through the graph to the downward forced variables. The advantage of this approach is that it splits the complex modeling of multiple variables varying in space and time into several simpler sub-models, first describing inter-variable dependencies then space-time variability. The next section describes how this approach is implemented in the case of agricultural droughts, hydrological droughts and fire weather.

### 3.2 Notation

Variables $\tilde{S}_{x,t}$, $\tilde{F}_{x,t}$ and $\tilde{Q}_{g,t}$ denote the observed values of SWI, FWI and Q, respectively, recorded at some spatial location (pixel $x$ for SWI and FWI, stream gauging station $g$ for Q) and some time step $t$.

Standardized anomalies are computed from the raw values by subtracting the interannual (1959-2023) monthly means and dividing by the interannual monthly standard deviations, after a log transformation. Taking FWI as an example, this can be formalized as follows:

$$F_{x,t} = \frac{\log\left(\tilde{F}_{x,t}\right) - \mu_{x,m(t)}}{\sigma_{x,m(t)}} \tag{1}$$

where $m(t)$ denotes the calendar month (between 1 and 12) associated with time step $t$, $\mu_{x,i}$ denotes the empirical mean of all transformed values $\log\left(\tilde{F}_{x,t}\right)$ recorded during month $i$, and $\sigma_{x,i}$ similarly denotes the empirical standard deviation of transformed values. The motivation for using standardized anomalies is to remove the infra-annual seasonal trend, and to make all variables dimensionless and hence easier to model and compare. The bottom panels of Figure 1 illustrate that standardized data indeed show much less seasonality and asymmetry than the raw data.

An overview of the model used to describe these standardized anomalies is provided in Figure 2. The model is based on the assumption that SWI anomalies are able to explain an important part of the variability of FWI and Q anomalies, in both space and time. This assumption is based on physical reasoning (dry soils are a precursor to both low flows and fire-prone weather) but also on an empirical observation: (SWI,FWI) and (SWI,Q) are much more correlated than (FWI,Q) (not shown). This reinforces the idea that the former pairs are linked by causal relationships, while the correlation between FWI and Q is merely a consequence of them having SWI as a common driver (this will be further ascertained in Section 4.1). This leads to proposing two separate regressions between (SWI,FWI) and (SWI,Q) (right part of Figure 2). The (SWI,FWI) regression is defined at the pixel scale, whereas catchment-averaged SWI values are used for the (SWI,Q) regression.

While these regressions are sufficient to compute conditional probabilities (e.g. of having extreme FWI and Q anomalies given that SWI anomalies are extreme), they are not sufficient to compute joint probabilities (e.g. of SWI, FWI and Q being extreme together). To achieve this, SWI also needs to be equipped with a probabilistic model that should vary in time to reflect past trends in SWI values. In addition, since we are interested in spatial extents, the model should also be able to describe spatial dependence in SWI values. This is achieved by means of a Principal Component Analysis (PCA), as will be described in Section 3.3.

All the regressions mentioned in Figure 2 are performed using Generalized Additive Models for Location, Scale and Shape (GAMLSS, Rigby and Stasinopoulos, 2005). In a nutshell, GAMLSS is an extension of linear regression where the distribution of the response variable conditionally on explanatory variables does not have to be Gaussian, and where all the parameters of this distribution can be modeled as linear or smooth functions of the explanatory variables. In this analysis, this will be useful to describe the variability in both the mean and the standard deviation of the data, and to allow for asymmetric distributions.

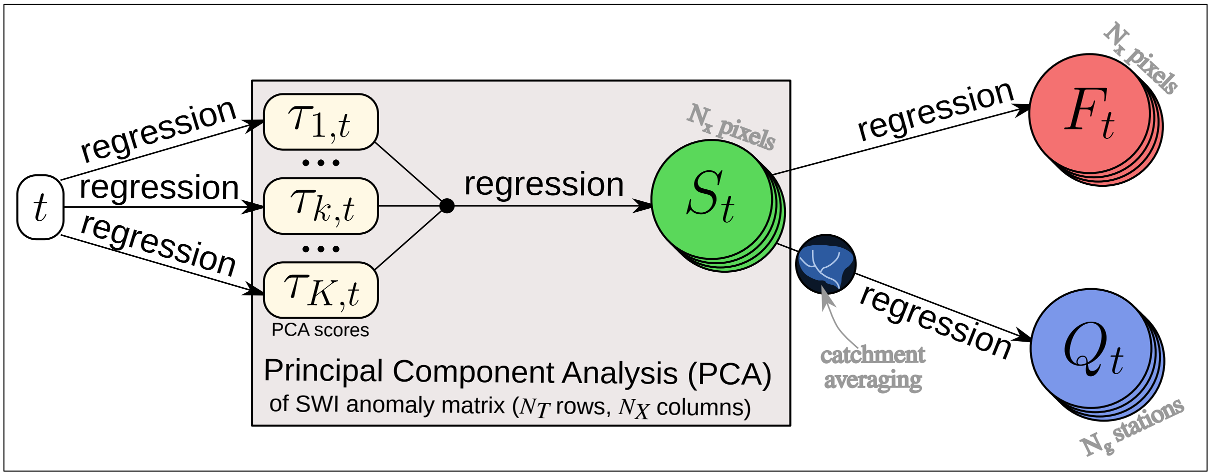

**Figure 2.** Probabilistic model overview.

### 3.3 Step 1: Principal Components of SWI anomalies

Standardized SWI anomalies $S_{x,t}$ are arranged in a $N_T \times N_X$ matrix, with $N_T = 65 \times 12 = 780$ monthly time steps and $N_X = 1103$ pixels, and a PCA is performed. This results in a set of $K$ components (the choice of $K$ will be discussed in section 4.1). Each component is a map $(\lambda_{k,x})_{x=1:N_X}$ referred to as component loadings. The time series of standardized SWI anomalies are then described by $K$ time series $(\tau_{k,t})_{t=1:N_T}$ (also known as component scores) corresponding to their projection onto the $K$ loadings.

In order to compute time-varying probabilities of occurrence, each times series $\tau_{k,t}$ is equipped with the following time-varying probabilistic model:

$$\begin{cases} \tau_{k,t} \sim \mathcal{SN}\left(\mu_{k,t}, \sigma_{k,t}, \nu_k\right) \\ \mu_{k,t} = \mathcal{P}\left(t; \boldsymbol{\alpha}_k^{(\tau)}\right) \\ log(\sigma_{k,t}) = \mathcal{P}\left(t; \boldsymbol{\beta}_k^{(\tau)}\right) \end{cases} \tag{2}$$

In equation 2, $\mathcal{SN}$ refers to the skew-normal distribution, which is favored over the standard normal distribution because component scores show noticeable asymmetry, as will be illustrated later (section 4.1). The location and scale parameters of this skew-normal distribution vary in time, while the shape parameter $\nu$ remains constant. Variability in time is induced by means of simple polynomial regressions with time, noted $\mathcal{P}(t; \boldsymbol{\alpha})$, which allow describing smooth but not necessarily linear or monotonic variations, as described next. We also assume independence between component scores ($\tau_{i,t} \perp \tau_{j,t'} \forall i \neq j$), which are already uncorrelated by construction of the PCA.

Polynomial regression is formally defined as shown in the equation below, where time $t$ is expressed in years and is centered:

$$\mathcal{P}\left(t;\boldsymbol{\alpha}\right)=\sum_{i=0}^{3}\alpha_i h_i(t)\text{ , with }\begin{cases}h_0(t)=1\\ h_1(t)=t\\ h_2(t)=t^2-1\\ h_3(t)=t^3-3t\end{cases}\tag{3}$$

In equation 3, $(h_i(t))_{i=0:3}$ are the first four Hermite polynomials and are favored over standard monomials $t$, $t^2$, $t^3$ because they lead to a better-behaved estimation due to their orthogonality properties (with respect to the Gaussian density). Alternative approaches such as splines could be used to describe smooth variations in time, but we found that they were more prone to estimation issues (e.g. optimization non-convergence) than the polynomial regression approach used here.

Finally, the temporal dependence affecting each score times series $\tau_{k,t}$ is accounted for using a Gaussian copula approach. Accounting for this temporal dependence is important to estimate the duration of extreme events. First, normal-transformed scores are defined as follows:

$$\epsilon_{k,t}=\Phi^{-1}\left(\Psi_{k,t}^{\mathcal{SN}}(\tau_{k,t})\right)\tag{4}$$

where $\Psi_{k,t}^{\mathcal{SN}}$ denotes the cumulative distribution function (cdf) of the skew-normal distribution in equation 2, and $\Phi^{-1}$ is the inverse cdf of a standard normal distribution $\mathcal{N}(0,1)$. The resulting time series $\boldsymbol{\epsilon}_{k,\boldsymbol{t}}=(\epsilon_{k,1},\ldots,\epsilon_{k,N_T})$ is then assumed to be a realization from a zero-mean multivariate Gaussian distribution with covariance $\boldsymbol{\Sigma}_\tau$ derived from some covariance function:

$$\boldsymbol{\epsilon}_{k,\boldsymbol{t}}\sim\mathcal{N}_{N_T}\left(\mathbf{0};\boldsymbol{\Sigma}_\tau\right)\tag{5}$$

For the case study in this paper, we use the covariance function of a first-order auto-regressive process (AR1), which exponentially decays with the lag $l$ between time steps:

$$C_\tau(l)=\rho^l\tag{6}$$

where $\rho$ is the lag-1 autocorrelation coefficient to be estimated.

### 3.4 Step 2: Local Regressions

As shown in Figure 2, the next step is to define a regression model predicting SWI anomalies $S_{x,t}$ from component scores $(\tau_{i,t})_{i=1:K}$. This is achieved by means of a simple Gaussian linear regression defined separately for each pixel $x$, which can be written as follows:

$$\begin{cases} S_{x,t} \sim \mathcal{N}\left(\mu_{x,t}, \sigma_x\right) \\ \mu_{x,t} = \alpha_{0,x}^{(S)} + \sum_{k=1}^{K} \alpha_{k,x}^{(S)} \tau_{k,t} \end{cases} \tag{7}$$

We restricted the model to such a simple linear regression structure because it is in fact the probabilistic model underpinning PCA (Tipping and Bishop, 1999). Temporal trends affecting PCA scores as defined by equation 2 will propagate to SWI anomalies through this regression.

Following Figure 2, the next step is to define the regression model predicting FWI anomalies $F_{x,t}$ from SWI anomalies at the same pixel $s_{x,t}$. We use again polynomial regressions acting on both the mean and the standard deviation, thereby allowing for a smooth but not necessarily linear or monotonic relation between FWI and SWI anomalies:

$$\begin{cases} F_{x,t} \sim \mathcal{N}\left(\mu_{x,t}, \sigma_{x,t}\right) \\ \mu_{x,t} = \mathcal{P}\left(s_{x,t}; \boldsymbol{\alpha}_x^{(F)}\right) \\ log(\sigma_{x,t}) = \mathcal{P}\left(s_{x,t}; \boldsymbol{\beta}_x^{(F)}\right) \end{cases} \tag{8}$$

Finally, the regression model for Q anomalies is similar, but it is applied at each station $g$ rather than pixel $x$ and uses catchment-averaged SWI anomalies $\bar{s}_{g,t}$ as input:

$$\begin{cases} Q_{g,t} \sim \mathcal{N}\left(\mu_{g,t}, \sigma_{g,t}\right) \\ \mu_{g,t} = \mathcal{P}\left(\bar{s}_{g,t}; \boldsymbol{\alpha}_g^{(Q)}\right) \\ log(\sigma_{g,t}) = \mathcal{P}\left(\bar{s}_{g,t}; \boldsymbol{\beta}_g^{(Q)}\right) \end{cases} \tag{9}$$

Accounting for spatial dependence is important for estimating the spatial extent of extreme events. The regression models in equations 7-9 do not include any explicit treatment of spatial dependence. This does not mean, however, that data are assumed spatially independent. Indeed, spatial dependence is induced in SWI by the use of a common set of covariates $(\tau_{i,t})_{i=1:K}$: pixels where estimated regression coefficients in equation 7 are similar will vary together, and hence be dependent. This spatial dependence may propagate to FWI and Q through the regressions in equations 8 and 9. We hypothesize that the common set of covariates explains most of the spatial dependence, leaving a residual spatial dependence which can be accounted for with a Gaussian copula approach. First, using FWI as an example (the treatment is identical for SWI and Q), normal-transformed data are defined as follows:

$$\varepsilon_{x,t} = \Phi^{-1}\left(\Psi_{x,t}^{\mathcal{N}}(f_{x,t})\right) \tag{10}$$

where $f_{x,t}$ is the observed FWI anomaly, $\Psi_{x,t}^{\mathcal{N}}$ is the cdf of the normal distribution in equation 8, and $\Phi^{-1}$ is the inverse cdf of a standard normal distribution $\mathcal{N}(0,1)$. The resulting spatial fields $\boldsymbol{\varepsilon}_{\boldsymbol{x},t} = (\varepsilon_{1,t}, \ldots, \varepsilon_{N_X,t})$ are then assumed to be realizations from a centered multivariate Gaussian distribution with covariance $\boldsymbol{\Sigma}_f$ derived from some covariance function:

$$\boldsymbol{\varepsilon}_{\boldsymbol{x},t} \sim \mathcal{N}_{N_X}\left(\mathbf{0};\boldsymbol{\Sigma}_f\right) \tag{11}$$

For the case study in this paper, we use an isotropic exponential covariance function that solely depends on the Euclidean distance $d$ between pixels:

$$C_f(d) = \exp\left(-d/\lambda\right) \tag{12}$$

where $\lambda > 0$ is a range parameter to be estimated.

### 3.5 Estimation and Stochastic Simulation

The approach described in the previous section builds on a combination of simple models. Parameter estimation is thus relatively straightforward and can rely on standard tools. Parameters for all regressions (i.e. $\boldsymbol{\alpha}$'s, $\boldsymbol{\beta}$'s, $\boldsymbol{\sigma}$'s and $\boldsymbol{\nu}$'s in equations 2, 7, 8 and 9) are estimated with the procedures implemented in `R` package `gamlss` (Stasinopoulos and Rigby, 2007), applied separately on each pixel (or station). Note that the Q dataset contains missing values, and the corresponding years are removed on a station-by-station basis before estimating the (SWI,Q) regression of equation 9. The AR1 parameter $\rho$ in equation 6 is estimated with the `arima` `R` function, and the range parameter $\lambda$ in equation 12 can be estimated by a least-square fit to pairwise correlations. For the latter, pairs of values of Q where at least one of the two values is missing are removed before computing the correlation.

Once all parameters have been estimated, it is possible to generate a replicated dataset by following Figure 2:

1. simulate PCA scores $(\tau_{k,t})$ from equation 2;
2. simulate SWI anomalies $(s_{x,t})$ given PCA scores using equation 7;
3. simulate FWI anomalies $(f_{x,t})$ given SWI anomalies using equation 8;
4. simulate Q anomalies $(q_{g,t})$ given SWI anomalies averaged over each catchement using equation 9;
5. transform SWI, FWI and Q anomalies back into natural space by inverting equation 1.

We repeated this procedure a thousand times for the analyses in this paper, generating enough replicated spatio-temporal datasets for extracting empirical probability estimates. For instance, the probability of jointly exceeding some (SWI,FWI,Q) thresholds over more than half of pixels/stations can be estimated by counting how many times this event occurred in the replicated datasets, and dividing by the number of replications.

## 4 Agricultural Droughts, Hydrological Droughts and Fire Weather in France

The probabilistic model described in the previous section 3 is applied to the French SWI, FWI and Q data described in section 2. After a description of model inference and checking (4.1), results are analysed in terms of at-site estimates, for each variable

https://doi.org/10.5194/egusphere-2026-1406
Preprint. Discussion started: 31 March 2026

separately (4.2) and for the three variables together (4.3). The spatial extents and average durations of extreme events are then analysed, both during the historical period (4.4) and in the future (4.5).

### 4.1 Model Estimation and Checking

As described in section 3, the first step is to perform a PCA of SWI anomalies. Figure 3(a)–(b) shows the scores and loadings for the first two components. The first component explains 57% of the total variance and affects most of the country, although loadings are noticeably lower around the Mediterranean coast. The second component explains 11% of the total variance and highlights a north-south gradient, with the highest loadings (in absolute value) concentrated around the Mediterranean coast. Four additional components are retained, reaching 80% of explained variance (see Supplementary Figure S2).

The pink lines in Figure 3(a)–(b) illustrate the estimated regression model of equation 2. Temporal variability is noticeable, especially a decreasing trend in the scores of the second component. There is no discernible edge effect in regression curves at the beginning or at the end of the 1959–2023 analysis period, probably thanks to the rather low degree of the polynomial. Figure 3(a) also highlights some asymmetry in the first component, with negative values showing an heavier tail than positive ones, thereby justifying the use of a skew-normal distribution (see also Supplementary Figure S3). Other hypotheses made by the model are found to be in agreement with the data, in particular the lack of seasonality in equation 2 (accounted for by the standardization of equation 1, see Figure S4) or the AR(1) temporal dependence model in equation 6 (see Supplementary Figure S5).

Figure 3(b–c) shows results for (SWI,FWI) and (SWI,Q) regressions at the Tarn example pixel/station. It highlights the non-linearity of the relations, which tend to flatten for large negative SWI values. It also highlights that standard deviations also depend on SWI (especially for Q). These observations are fairly consistent across all pixels/stations (see Supplementary Figure S6) and justify the need to go beyond simple linear regression and to use GAMLSS.

While the regressions (SWI,FWI) and (SWI,Q) illustrated in Figure 3(b–c) induce a dependence between these variable pairs, there is no such explicit regression model to induce a dependence for the (FWI,Q) pair. Yet this dependence does exist and is induced by the fact that both variables depend on SWI. This is illustrated in Figure 4: FWI and Q anomalies are clearly correlated (panel (a), correlation $\sim -0.6$), but scatterplots stratified by SWI anomalies, representing the conditional distributions of FWI,Q$|$SWI $= x$, do not show any sign of dependence (panel (b)). In statistical terms, this means that FWI and Q anomalies are dependent, but they are independent conditionally on SWI. This behavior is consistent across all stations: (FWI,Q) correlations are around $-0.6$ on average, but their partial correlations (i.e. after the effect of SWI has been removed) drop to $\sim -0.1$ (see Supplementary Figure S7).

### 4.2 At-site Distributions

Figure 5 shows the time-varying distribution of SWI, FWI and Q at the Tarn pixel/station. Trends in time are apparent and are induced by trends in the PCA scores (Figure 3(a)–(b)). At this location, the 2022 event appears to be quite extreme in terms of SWI and Q (close to the 5%-quantile), less so in terms of FWI.

https://doi.org/10.5194/egusphere-2026-1406
Preprint. Discussion started: 31 March 2026

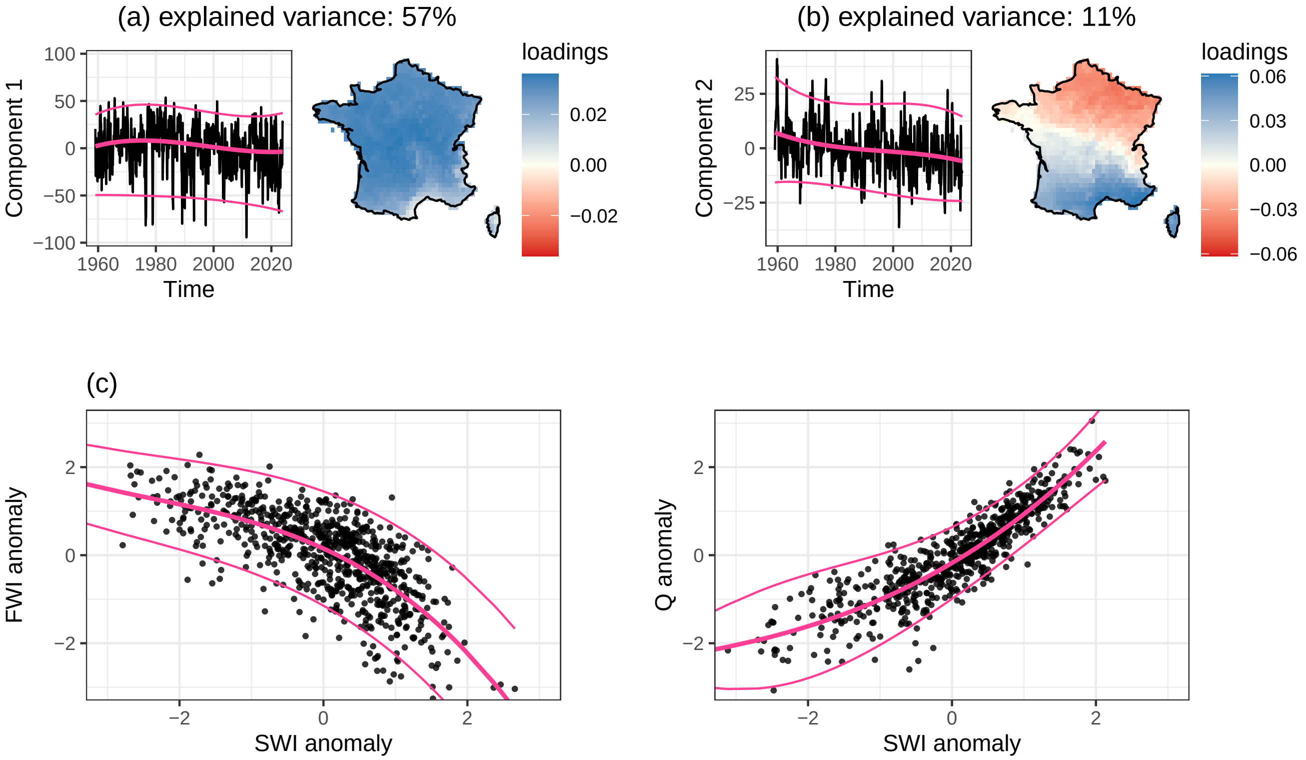

**Figure 3.** Estimated GAMLSS models. (a) Scores (time series) and loadings (map) associated with the first principal component. The thick pink line shows the median of the GAMLSS model fitted to the PCA score time (equation 2), whereas thin lines represent the 95% probability interval. (b) Same as (a) for the second component. (c) GAMLSS models for the pairs (SWI,FWI) (left, equation 8) and (SWI,Q) (right, equation 9) at the Tarn example pixel/station. Pink lines represent the conditional median (thick) and the conditional 95% probability interval (thin).

Figure 6 evaluates the goodness-of-fit at all pixels/stations by means of PP-plots (i.e. empirical cdf of $\Psi_t(o_t)$, where $\Psi_t$ is the cdf of the time-varying distribution shown in Figure 5 at time $t$ and $o_t$ is the corresponding observation). For SWI and FWI, most curves remain close to the diagonal, indicating an acceptable fit. There is, however, a systematic tendency to slightly under- and over-estimate SWI and FWI, respectively, the cause of which needs to be further investigated. Larger departures are visible at a few stations for Q. A closer inspection reveals that most of these poor-fit stations are located either in groundwater-dominated northern regions or in mountainous areas. In both cases, the SWI-Q relationship is poorly captured because streamflow is not driven by soil moisture in these regions, but rather by deep aquifers or snowmelt.

Having a time-varying distribution at all pixels/stations allows estimating the probability of crossing some threshold (downward for SWI and Q, upward for FWI) everywhere and at any time. Figure 7 hence shows the probability of exceeding the

https://doi.org/10.5194/egusphere-2026-1406
Preprint. Discussion started: 31 March 2026

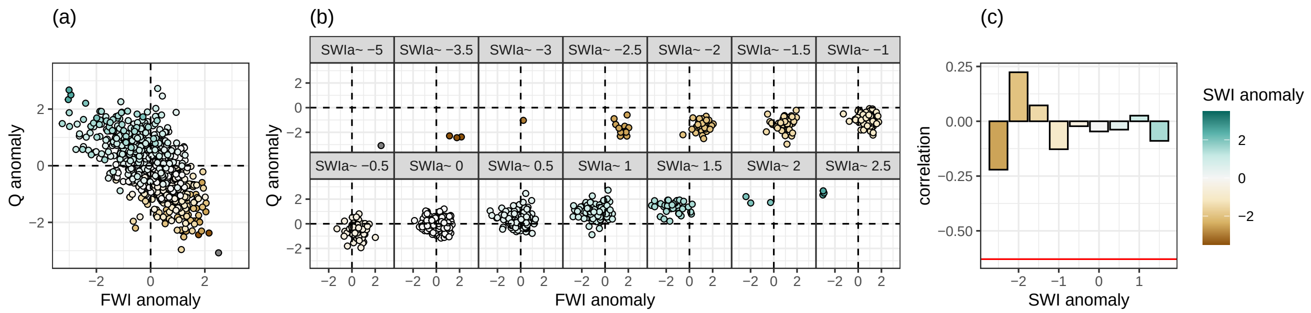

**Figure 4.** Dependence between FWI and Q anomalies at the Tarn example pixel/station. (a) Full scatterplot. (b) Conditional scatterplots: SWIa $\sim x$ means that SWI anomalies are in the interval $x \pm 0.25$ . (c) Conditional correlations (bars), computed for each group in panel (b) containing at least 10 observations, compared with the full correlation (horizontal line) computed from panel (a).

2022 annual minima (SWI, Q) or maxima (FWI). It indicates that the 2022 event was extreme in terms of SWI (probabilities of occurrence well below 0.1 at many pixels), less so in terms of FWI and Q, at least locally. It also suggests that temporal trends have made this event less unlikely in 2022 than it would have been in 1959.

### 4.3 Multivariate At-site Distributions

Figure 8 shows that the bivariate distributions induced by the model are consistent with the observed scatterplots, indicating that the (SWI,FWI) and (SWI,Q) regressions are able to adequately represent all pairwise dependencies in the triplet (SWI,FWI,Q) (at least at this Tarn example pixel/station).

Moving from bivariate to trivariate distributions, Figure 9(a) shows the observed joint frequency of crossing (SWI,FWI,Q) thresholds, and suggests that this joint frequency behaves neither as in the independent nor the perfectly dependent cases. Note that the few curves exceeding the ‘perfect dependence‘ line can be explained by missing values in Q data: thresholds are computed using all available data for each variable, but joint frequencies are computed using (SWI,FWI,Q) triplets where all three variables are available together. Figure 9(b) shows the corresponding joint probabilities estimated by the model, and suggests that the model adequately reproduces the behavior of observations, although the slightly higher curves may suggest a slight tendency to over-estimation. Note that a few curves exceed the ‘perfect dependence‘ line again, due to the fact that the thresholds are computed on observations, and their modelled probability of (non)exceedance is hence not exactly equal to $p$. Figure 9(b) indicates that the estimated joint probabilities are much higher than the probabilities computed under the independence assumption: as an order of magnitude, for $p = 0.1$, the former is on average 10 times higher than the latter. An evaluation of dependence focusing on extremes (i.e. when $p \rightarrow 0$) can also be performed (Coles et al., 1999), and it suggests an asymptotic independence behavior (see Supplementary Figure S8).

Having a trivariate distribution enables a multi-hazard characterization of the severity of the 2022 event. Note that this characterization is time-dependent, since the trivariate distribution upon which it is based varies in time (Supplementary Figure

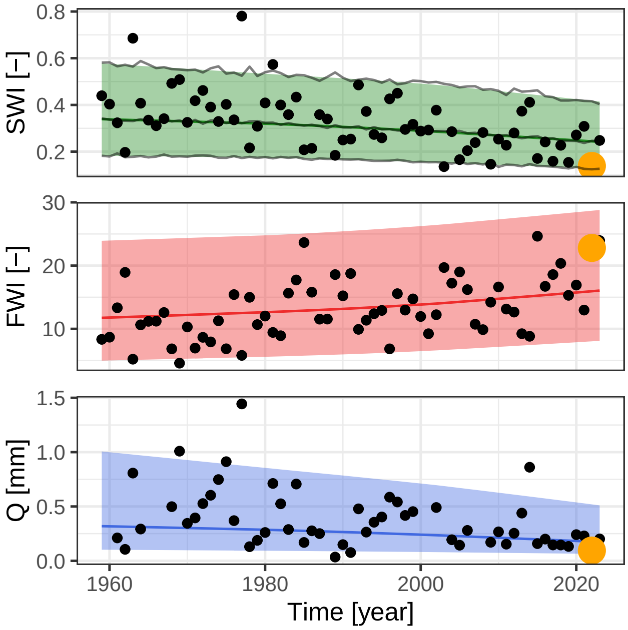

**Figure 5.** Time-varying distributions for annual minimum SWI, annual maximum FWI and annual minimum Q at the Tarn example pixel/station. Points are observations, with the larger golden point highlighting the year 2022. The thick line shows the estimated median, and the filled area extends between the 0.05 and 0.95 quantiles. The gray lines in the top panel show the raw empirical median and quantiles obtained from 1000 Monte-Carlo replications, smoothed in subsequent figures.

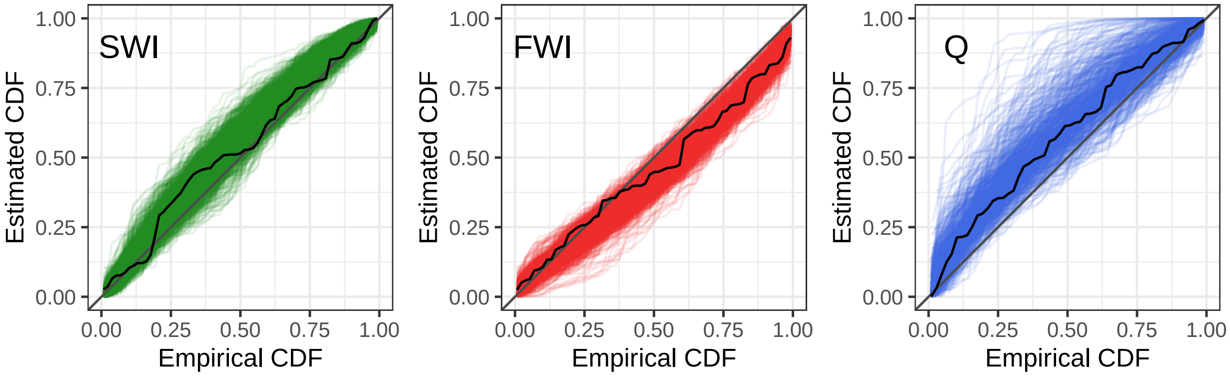

**Figure 6.** Probability-Probability plots to evaluate goodness of fit of time-varying distributions for annual minimum SWI, annual maximum FWI and annual minimum Q. Each line represents a pixel/station, and the black line corresponds to the data shown in Figure 5

https://doi.org/10.5194/egusphere-2026-1406
Preprint. Discussion started: 31 March 2026

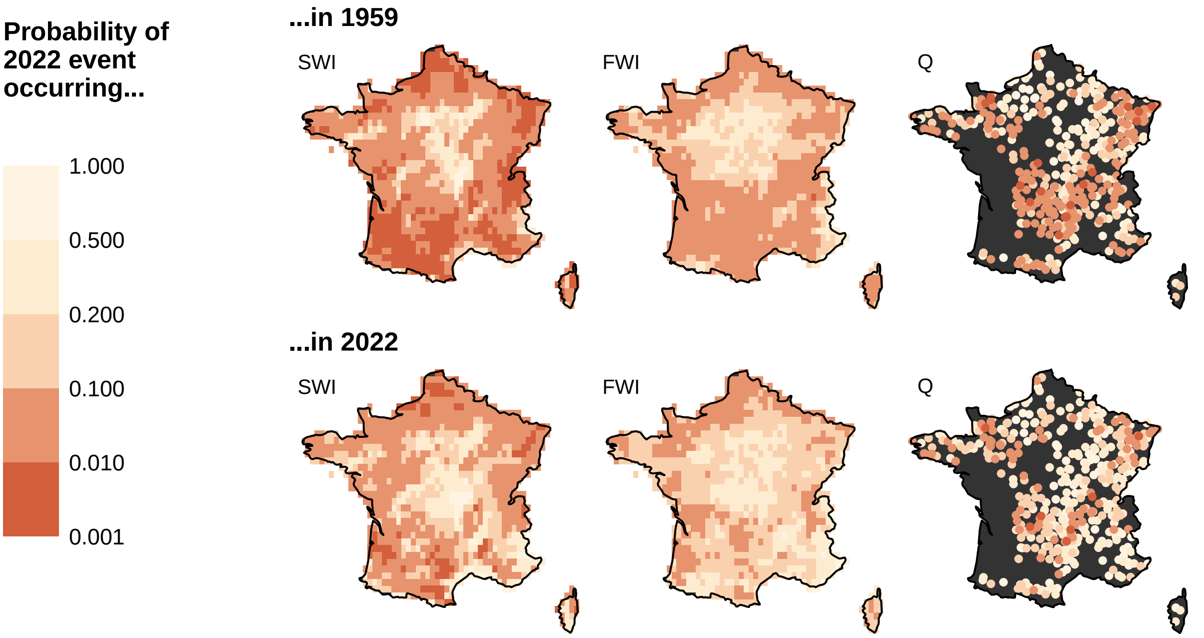

**Figure 7.** Probability of exceeding the intensity of the 2022 event in terms of SWI, FWI and Q, at two different dates.

S9). Figure 9(c) indicates that the 2022 event could be considered as extreme in terms of (SWI,FWI,Q) nearly everywhere in France when it occurred (median probability $\approx 0.01$), which was not the case when each variable was considered separately. This is a partly expected result since the probability of a multi-hazard event is necessarily smaller than the probabilities of the individual single-hazard events. This median probability of $\approx 0.01$ (corresponding to a 100-year event) can also be compared to the median probability computed under the independence hypothesis, which is around 20 times smaller (corresponding to a 2000-year event). This shows that modeling stochastic dependence is critical for an appropriate assessment of compound hazards.

## 4.4 Spatial Extent of Extreme Events

The spatial extent of droughts and fire-prone conditions can be quantified by computing the percentage of pixels/stations crossing a low (SWI,Q) or a high (FWI) threshold, taken here as the empirical 5-year event computed from the observation period (1959-2023). These spatial extents are just percentages and do not account for the forest cover of each pixel (FWI) or the area controlled by each catchment (Q). Figure 10 shows the observed spatial extents, and indicate that the 2022 spatial extent is extreme, even unprecedented over the period 1959–2023, for all three variables, despite the fact that at-site values of Q and FWI are not extreme (Figure 5 and Figure 7).

Figure 10 also shows the estimated time-varying distribution of annual maximum extent for the three variables. Dotted lines correspond to ignoring the residual spatial dependence model of equation 11. This does not make any marked difference for

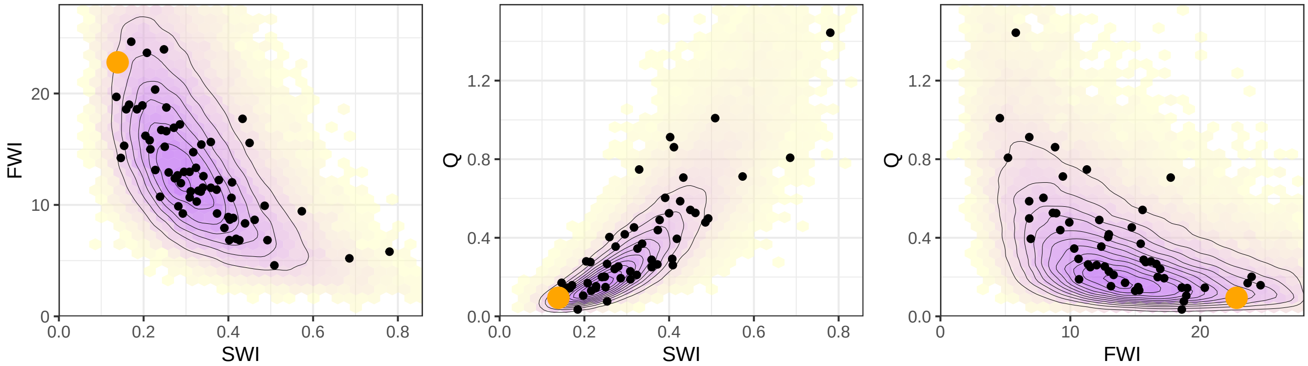

**Figure 8.** Pairwise joint distribution of annual minimum SWI, annual maximum FWI and annual minimum Q at the Tarn example pixel/station. Points denote observed values, the larger golden point denotes 2022, the underlying color denotes the joint bivariate pdf estimated by hexagonal binning of 1000 Monte-Carlo replications, and thin lines corresponding contours.

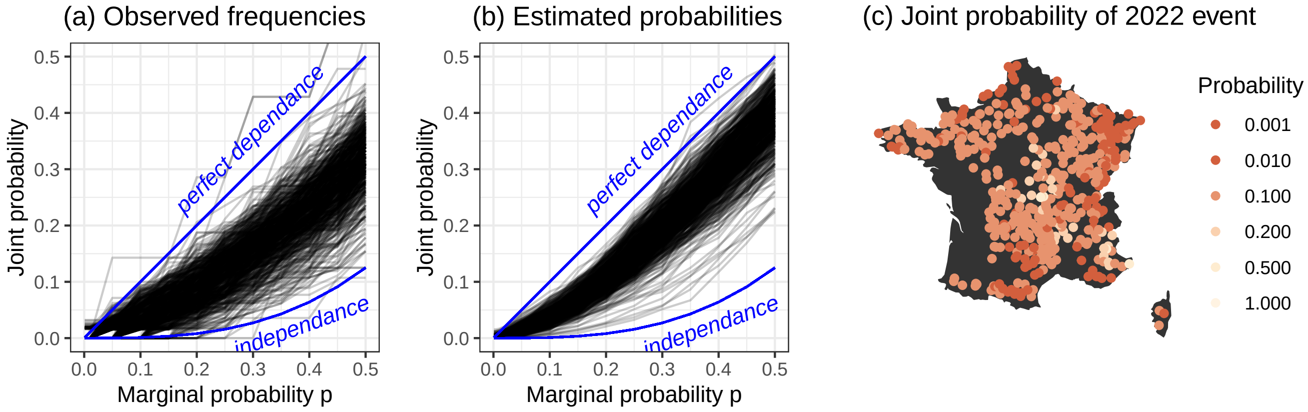

**Figure 9.** Joint distribution of annual minimum SWI, annual maximum FWI and annual minimum Q. (a) Observed frequencies of jointly nonexceeding SWI and Q $p$-quantiles and exceeding FWI $(1-p)$-quantile, as a function of $p$. Each black line corresponds to one station, and blue lines correspond to the cases of independence $(y = p^3)$ and perfect dependence $(y = p)$. (b) Same as (a) but for joint probabilities rather than observed joint frequencies, estimated using 1000 Monte-Carlo replications. (c) Probability of jointly exceeding the intensity of the 2022 event for all three variables (SWI,FWI,Q), computed in 2022.

https://doi.org/10.5194/egusphere-2026-1406
Preprint. Discussion started: 31 March 2026

SWI, suggesting that spatial dependence is already adequately captured by the first 6 principal components. By contrast, when residual spatial dependence is ignored, the estimated distribution of FWI spatial extents is much less variable and hence cannot capture the large spatial extents that are frequently observed (see also PP-plots in Supplementary Figure S10). The spatial dependence that propagates from SWI to FWI through the (SWI,FWI) regression is hence not sufficient to explain the observed amount of spatial dependence in FWI, hence requesting the additional dependence component embedded in equation 11. Q qualitatively behaves as FWI, but the amount of "missing" spatial dependence is much smaller.

The bottom panel of Figure 10 characterizes the 2022 event in terms of spatial extent and confirms that it was extreme in this respect for all three variables, even for FWI and Q which where less extreme when considered locally (Figure 7). The figure also shows a non-linear increase of this probability during the 1959–2023 period indicating that such events are becoming less unlikely as time progresses: depending on the variable, the probability of occurrence increased by a factor ranging between 2 and 5 during the observation period, highlighting the need to consider a continuous temporal evolution of probabilities, as opposed to constant probabilities associated with predefined periods.

Note that in addition to the spatial extent of extreme events, their duration can also be of interest. Supplementary Figure S11 shows results for durations and indicates that their behavior is qualitatively similar to that of spatial extents.

### 4.5 Future Projections

We conclude this case study by demonstrating how the probabilistic model can be used for future projections. Each climate model listed in Table 1 provides spatial SWI fields up to year 2099. These fields can be projected into the PCA basis identified in section 4.1, leading to a new set of PCA scores time series. Since the PCA model of equation 2 varies in time, it needs to be re-estimated to reflect the new PCA scores that extend up to 2099, including parameters for both the polynomial regressions (equation 2) and the AR(1) temporal dependence (equation 6). Once the PCA model is re-estimated, the Monte-Carlo procedure of section 3.5 can be used to generate many spatio-temporal (SWI,FWI,Q) datasets: PCA scores are first generated, then SWI values given the scores using equation 2, then FWI and Q values given SWI values using equations 8 and 9. Note that the latter two models are not re-estimated since they do not vary in time, which effectively assumes that inter-variable dependencies will not change in the future. The many replicated (SWI,FWI,Q) datasets enable the estimation of probabilities in the same way as illustrated previously for the observation period. Note that the approach described here only uses the SWI variable from the climate model, due to the fact that SWI is the root variable in the causal diagram of Figure 2. However, it uses neither FWI (which could easily be computed from climate model outputs) nor Q (which is not provided by climate models and would necessitate an impact modelling chain).

Figure 11 shows the time-varying probability of exceeding the 2022 extent (top) and duration (bottom), as projected by each climate model up to year 2099. In a nutshell, this figure suggests that the 2022 event may become a frequent event by the end of the century, both in terms of spatial extent and duration. This statement needs to be qualified by a tendency to over-estimate the probability estimated from observations, with some climate models widely overshooting during the observed period (e.g. models 4, 8 and 11 in Table 1). Also note the specific behavior of FWI spatial extent: the probability of exceeding the 2022

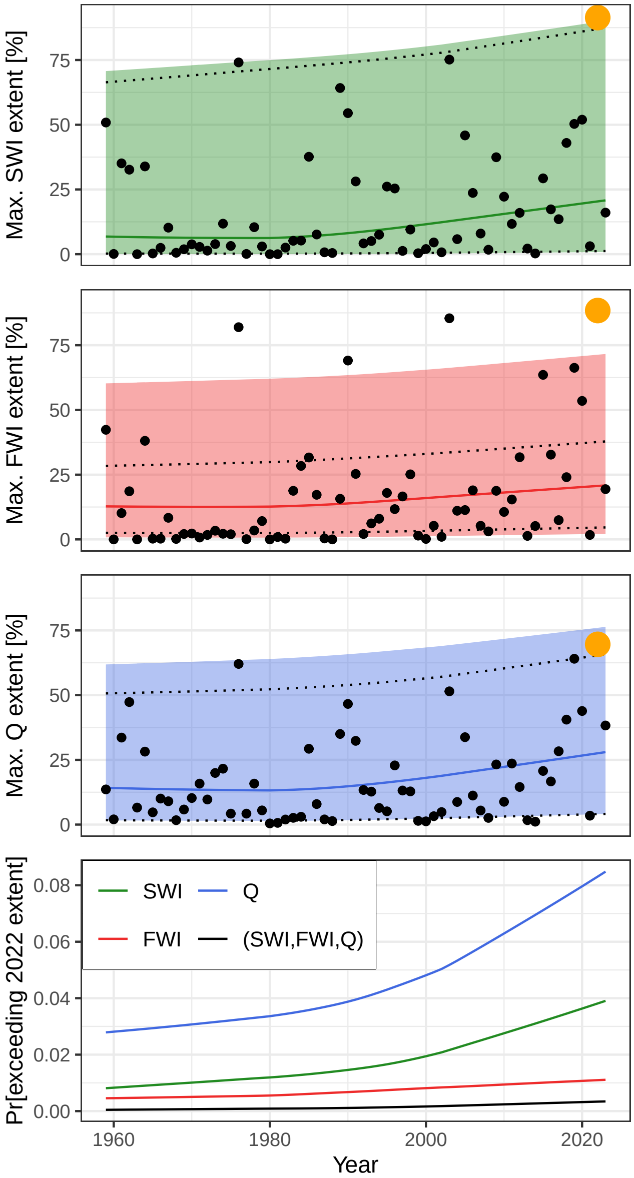

**Figure 10.** Time-varying distribution of the annual maximum spatial extent of SWI, FWI and Q events (top three panels), and time-varying probability of exceeding the spatial extent of the 2022 event for each variable individually and jointly (bottom panel). Points are observations, with the larger golden point highlighting the year 2022. The thick line shows the estimated median, and the filled area extends between the 0.05 and 0.95 quantiles. The dotted lines show the quantiles obtained with a model ignoring residual spatial dependence (equation 12).

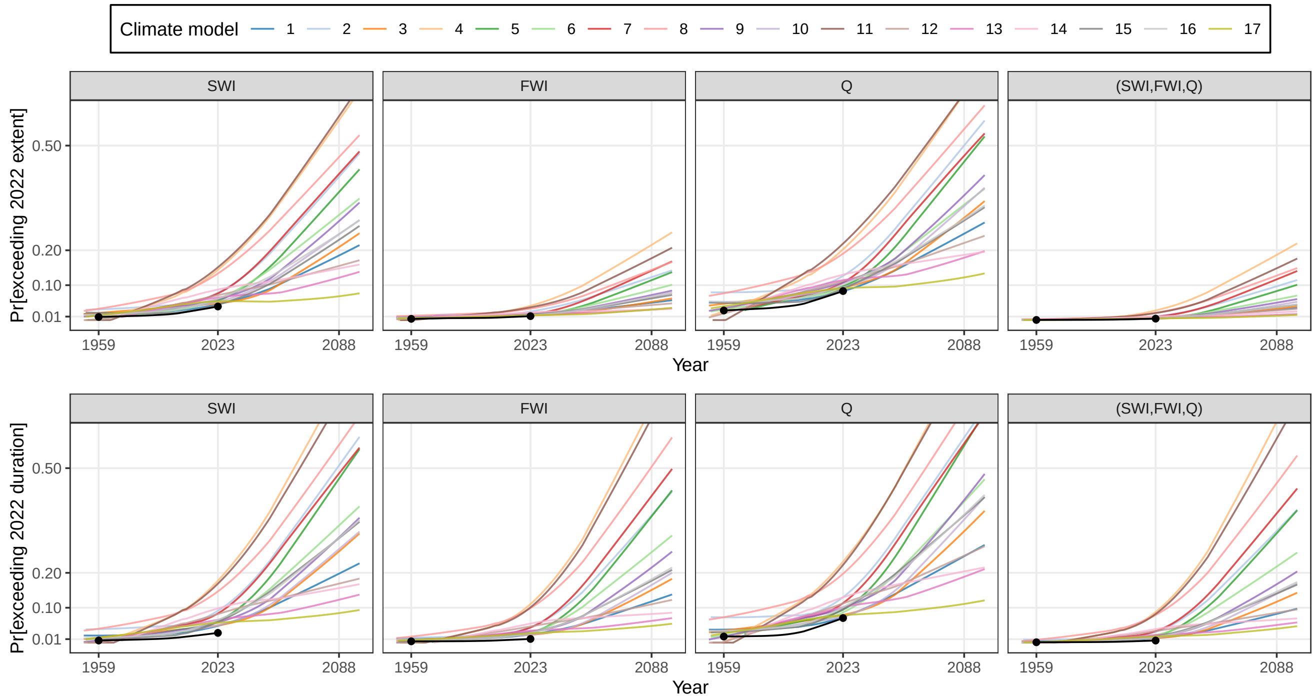

**Figure 11.** Time-varying probability of exceeding the spatial extent (top) and the duration (bottom) of the 2022 event for each variable individually and jointly, as projected by 17 GCM/RCM combinations. The thick lines correspond to the observations-based estimates based on the period 1959–2023 (Figure 10)

value increases much less sharply that for other variables, so that the 2022 FWI extent remains fairly extreme even by 2099 standards.

## 5 Discussion

The analysis of future projections presented in the previous section solely aimed at demonstrating that the proposed probabilistic model can be used for this purpose. However this analysis remains quite superficial and could be extended in several directions in future work. For instance, the results could be compared with the ones obtained using future projections from a whole hydroclimatic modeling chain (including in particular hydrological models to provide future Q from climate model outputs). The ability of climate models to reproduce the observed climate should also be further analyzed, along with the various sources of projection uncertainty (GCM vs. RCM in particular). Alternatively, applying the proposed model to GCM+RCM historical simulations, with and without anthropogenic greenhouse gas emissions, would enable a compound event attribution analysis.

https://doi.org/10.5194/egusphere-2026-1406
Preprint. Discussion started: 31 March 2026

The proposed model could also be extended in several directions. First, alternative space/time covariance functions could be considered, to account for long-memory processes or space/time nonstationarity of covariances. While the case study results did not suggest a need to go beyond the simple covariance functions used here, other applications with different variables may require to do so, and the sensitivity of the results to the selected covariance functions should be further appraised. More generally, the applicability of the proposed model to different variables needs to be assessed. The three variables used in this paper are fairly smooth in space and can be considered at a relatively coarse monthly time step. Variables that are varying much more rapidly in space and time (typically, floods, extreme precipitations or actual fires), or data considered at a finer space/time resolution, are probably less amenable to the combination of simple models used in this paper. An interesting advantage of the proposed approach is that it generalizes fairly easily to more than three variables, as long as one is able to establish a causal diagram such as the one in Figure 2.

A drawback of the proposed approach is that combining simple conditional models does not allow explicitly controlling important properties of extremes, such as the tail behavior of individual variables (heavy or light tails?) or the nature of joint distributions (both between variables and in space), for instance in terms of asymptotic dependence vs. asymptotic independence. In fact, these properties depend on the many choices made in the sub-models, in particular the various regressions of sections 3.3 and 3.4: distribution family, formulation of the regression, etc. For the variables studied in this paper, both the data and the model appear to follow an asymptotic independence behavior, but other variables might behave differently. Theoretical guidance from the statistical community would be useful to select regression models depending on the desired extremal behavior.

A technical difficulty of the proposed approach is that the Monte-Carlo-based estimation of probabilities is prone to memory issues. The observed dataset comprises around $2.2 \times 10^6$ values. With 1000 replications, this increases to $2.2 \times 10^9$, and nearly $5 \times 10^9$ values per climate model when considering future projections. This roughly corresponds to the available memory of current personal computers, but memory issues would be unavoidable with alternative datasets having finer spatial/temporal resolution, or a continental/global extent. These may require tailored data-processing workflows, but these are not straightforward to implement because some variables require keeping full spatial fields in memory while others require keeping full time series. Alternatively, analyses may need to be run on computing clusters providing a larger memory.

The results confirm the exceptional nature of the 2022 drought in France, characterized not only by its intensity but also by its unusually large spatial extent as reported previously in continental scales analyses (Meng et al., 2023; Bevacqua et al., 2024). This is also consistent with the large-scale persistent anticyclonic anomaly over Western Europe found in Faranda et al. (2023).

Finally, the way the proposed model could be turned into an operational tool remains to be defined. A difficulty is that in France, the three hazards are managed by distinct agencies, hence not facilitating the evaluation of compound-hazard strategies. However, the communities impacted by the different hazards generally show a strong overlap, and their resilience may be affected by the joint occurrence of several hazards, especially if they are long or widespread. Possible operational uses of the proposed model include multivariate seasonal forecasting (e.g. for reservoir management) and the design of disaster response infrastructures (e.g. distributed water storage for fire protection in the context of declining low flows).

https://doi.org/10.5194/egusphere-2026-1406
Preprint. Discussion started: 31 March 2026

## 6 Conclusions

Characterizing multi-faceted events such as the exceptionally warm and dry year 2022 in France requires a joint probabilistic model for several spatialized variables. This paper demonstrates how such a model can be built by combining relatively simple ingredients: a PCA to describe the bulk of spatial dependence, regressions to describe inter-variable dependences, and basic covariance functions to describe residual spatial dependence and autocorrelation. The advantages of such a modular approach are that it breaks down a complex problem into several simpler sub-problems and makes estimation fairly straightforward.

Our national-scale analysis in France suggests that the proposed approach is adequate for three monthly variables that vary fairly smoothly in space: SWI, FWI and Q. Model checking indicates a reliable description of the time-varying local distributions of each variable as well as the local trivariate distributions. Moreover, space-time properties such as the spatial extent and the duration of extreme events are also reliably reproduced.

Thanks to this probabilistic model, the 2022 event can be characterized from different points of view. When considered locally, the 2022 event was extreme in terms of SWI at many locations, but was more moderate in terms of FWI and Q. However, the 2022 event was found to be extreme nearly everywhere in France when the three variables are considered together. Likewise, both the duration and the spatial extent of the 2022 event was found to be extreme for all three variables. Underlying trends in the three variables during the historical period have progressively increased the likelihood of such events, and future projections indicate that this event may become even more frequent by the end of the century.

Improved understanding of how these three hazards may change at regional and global scales will be crucial for both advancing scientific knowledge and informing practical strategies to address future drought challenges.

*Code and data availability.* The codes and data used in this paper are available in the following repository: https://zenodo.org/records/18922524

*Video supplement.* The data analyzed in this paper have been animated and sonified in the video available at https://vimeo.com/1078937179

*Author contributions.* All authors contributed to conceptualization and methodology development. BR and RB prepared the manuscript with contributions from all co-authors. BR implemented the data analysis. BR, RB and JPV acquired funding.

*Competing interests.* The authors declare that they have no conflict of interest.

*Acknowledgements.* This work received financial support from INRAE as part of the XRISQUES Metaprogramme. We acknowledge the World Climate Research Programme's Working Group on Regional Climate, and the Working Group on Coupled Modelling, former coordinating body of CORDEX and responsible panel for CMIP5. We also thank the climate modelling groups (listed in Table 1 of this paper) for producing and making available their model output. We also acknowledge the Earth System Grid Federation infrastructure an international effort led by the U.S. Department of Energy's Program for Climate Model Diagnosis and Intercomparison, the European Network for Earth System Modelling and other partners in the Global Organisation for Earth System Science Portals (GO-ESSP). Finally, we thank Météo France for making the SAFRAN dataset available and the Ministry of Ecological Transition for making streamflow data available.

## References

Abatzoglou, J. T., Dobrowski, S. Z., and Parks, S. A.: Multivariate climate departures have outpaced univariate changes across global lands, Scientific Reports, https://doi.org/10.1038/s41598-020-60270-5, 2020.

Angélil, O., Stone, D., Perkins-Kirkpatrick, S., Alexander, L. V., Wehner, M., Shiogama, H., Wolski, P., Ciavarella, A., and Christidis, N.: On the nonlinearity of spatial scales in extreme weather attribution statements, Climate Dynamics, 50, 2739–2752, https://doi.org/10.1007/s00382-017-3768-9, 2018.

Bevacqua, E., Rakovec, O., Schumacher, D. L., Kumar, R., Thober, S., Samaniego, L., Seneviratne, S. I., and Zscheischler, J.: Direct and lagged climate change effects intensified the 2022 European drought, Nature Geoscience, https://doi.org/10.1038/s41561-024-01559-2, 2024.

Biella, R., Shyrokaya, A., Ionita, M., Vignola, R., Sutanto, S. J., Todorovic, A., Teutschbein, C., Cid, D., Llasat, M. C., Alencar, P., Matanó, A., Ridolfi, E., Moccia, B., Pechlivanidis, I., van Loon, A., Wendt, D. E., Stenfors, E., Russo, F., Vidal, J.-P., Barker, L., de Brito, M. M., Lam, M., Bláhová, M., Trambauer, P., Hamed, R., McGrane, S. J., Ceola, S., Bakke, S. J., Krakovska, S., Nagavciuc, V., Tootoonchi, F., Di Baldassarre, G., Hauswirth, S., Maskey, S., Zubkovych, S., Wens, M., and Tallaksen, L. M.: The 2022 drought needs to be a turning point for European drought risk management, Natural Hazards and Earth System Sciences, 25, https://doi.org/10.5194/nhess-25-4475-2025, 2025.

Cattiaux, J. and Ribes, A.: Defining Single Extreme Weather Events in a Climate Perspective, Bulletin of the American Meteorological Society, 99, 1557–1568, https://doi.org/10.1175/BAMS-D-17-0281.1, 2018.

Christidis, N., Jones, G. S., and Stott, P. A.: Dramatically increasing chance of extremely hot summers since the 2003 European heatwave, Nature Climate Change, 5, 46–50, https://doi.org/10.1038/nclimate2468, 2015.

Coles, S., Heffernan, J. E., and Tawn, J. A.: Dependence measures for extreme value analyses, Extremes, 2, 1999.

Commissariat général au développement durable: Sécheresse de 2022 : des coûts estimés à plus de 5 milliards d'euros, Théma Essentiel 37, Ministère de la Transition écologique, https://www.ecologie.gouv.fr/sites/default/files/publications/thema_essentiel_37_secheresse_2022_avril2025.pdf, 2025.

Copernicus Climate Change Service: European State of the Climate 2022, Tech. rep., Copernicus, https://doi.org/10.24381/GVAF-H066, 2023.

Cramer, W., Guiot, J., Fader, M., Garrabou, J., Gattuso, J.-P., Iglesias, A., Lange, M. A., Lionello, P., Llasat, M. C., Paz, S., Peñuelas, J., Snoussi, M., Toreti, A., Tsimplis, M. N., and Xoplaki, E.: Climate change and interconnected risks to sustainable development in the Mediterranean, Nature Climate Change, https://doi.org/10.1038/s41558-018-0299-2, 2018.

Deng, S., Zhao, D., Chen, Z., Liu, L., Zhu, Y., Wang, K., Gao, X., Wu, H., and Zheng, D.: Global Distribution and Projected Variations of Compound Drought-Extreme Precipitation Events, Earth's Future, https://doi.org/10.1029/2024EF004809, 2024.

Faranda, D., Pascale, S., and Bulut, B.: Persistent anticyclonic conditions and climate change exacerbated the exceptional 2022 European-Mediterranean drought, Environmental Research Letters, 18, https://doi.org/10.1088/1748-9326/acbc37, 2023.

Jacob, D., Petersen, J., Eggert, B., Alias, A., Christensen, O. B., Bouwer, L., Braun, A., Colette, A., Déqué, M., Georgievski, G., Georgopoulou, E., Gobiet, A., Menut, L., Nikulin, G., Haensler, A., Hempelmann, N., Jones, C., Keuler, K., Kovats, S., Kröner, N., Kotlarski, S., Kriegsmann, A., Martin, E., Meijgaard, E., Moseley, C., Pfeifer, S., Preuschmann, S., Radermacher, C., Radtke, K., Rechid, D., Rounsevell, M., Samuelsson, P., Somot, S., Soussana, J.-F., Teichmann, C., Valentini, R., Vautard, R., Weber, B., and Yiou, P.: EURO-

CORDEX: new high-resolution climate change projections for European impact research, Regional Environmental Change, 14, 563–578, https://doi.org/10.1007/s10113-013-0499-2, 2014.

Jacquemin, G., Allard, D., Freulon, X., and Vrac, M.: Return Period of Nonconcurrent Climate Compound Events: A Nonparametric Bivariate Generalized Pareto Approach, Environmetrics, 37, 2026.

Keeping, T., García García, D., Trigo, R., Santos, F. L., Barnes, C., Vahlberg, M., Meyer, R., Otto, F., Philip, S., Singh, R., Casas Osorio, S., Neves, M., and Haro, P.: Extreme fire weather conditions in Spain and Portugal now common due to climate change, Tech. rep., World Weather Attribution, https://doi.org/10.25560/123547, 2025.

Kirchmeier-Young, M. C., Wan, H., Zhang, X., and Seneviratne, S. I.: Importance of Framing for Extreme Event Attribution: The Role of Spatial and Temporal Scales, Earth's Future, 7, 1192–1204, https://doi.org/10.1029/2019EF001253, 2019.

Lanet, M., Li, L., Ehret, A., Turquety, S., and Treut, H. L.: Attribution of summer 2022 extreme wildfire season in Southwest France to anthropogenic climate change, npj Climate and Atmospheric Science, 7, https://doi.org/10.1038/s41612-024-00821-z, 2024.

Le Moigne, P., Besson, F., Martin, E., Boé, J., Boone, A., Decharme, B., Etchevers, P., Faroux, S., Habets, F., Lafaysse, M., Leroux, D., and Rousset-Regimbeau, F.: The latest improvements with SURFEX v8.0 of the Safran–Isba–Modcou hydrometeorological model for France, Geoscientific Model Development, https://doi.org/10.5194/gmd-13-3925-2020, 2020.

Leach, N. J., Li, S., Sparrow, S., van Oldenborgh, G. J., Lott, F. C., Weisheimer, A., and Allen, M. R.: Anthropogenic Influence on the 2018 Summer Warm Spell in Europe: The Impact of Different Spatio-Temporal Scales, Bulletin of the American Meteorological Society, 101, S41–S46, https://doi.org/10.1175/BAMS-D-19-0201.1, 2020.

Manning, C., Widmann, M., Bevacqua, E., Loon, A. F. V., Maraun, D., and Vrac, M.: Increased probability of compound long-duration dry and hot events in Europe during summer (1950–2013), Environmental Research Letters, 14, https://doi.org/10.1088/1748-9326/ab23bf, 2019.

Marson, P., Corre, L., Soubeyroux, J.-M., Sauquet, E., Robin, Y., Vrac, M., and Dubois, C.: Explore2 – Rapport de synthèse sur les projections climatiques régionalisées, Tech. rep., METEO FRANCE ; INRAE ; Institut Pierre-Simon Laplace, https://doi.org/10.57745/H88ES2, 2024.

Meng, Y., Hao, Z., Zhang, Y., and Feng, S.: The 2022-like compound dry and hot extreme in the Northern Hemisphere: Extremeness, attribution, and projection, Atmospheric Research, https://doi.org/10.1016/j.atmosres.2023.107009, 2023.

Philip, S., Kew, S., van Oldenborgh, G. J., Otto, F., Vautard, R., van der Wiel, K., King, A., Lott, F., Arrighi, J., Singh, R., and van Aalst, M.: A protocol for probabilistic extreme event attribution analyses, Advances in Statistical Climatology, Meteorology and Oceanography, https://doi.org/10.5194/ascmo-6-177-2020, 2020.

Quilcaille, Y., Gudmundsson, L., and Seneviratne, S. I.: Extending MESMER-X: a spatially resolved Earth system model emulator for fire weather and soil moisture, Earth System Dynamics, https://doi.org/10.5194/esd-14-1333-2023, 2023.

Ribes, A., Boé, J., Qasmi, S., Dubuisson, B., Douville, H., and Terray, L.: An updated assessment of past and future warming over France based on a regional observational constraint, Earth System Dynamics, 13, 1397–1415, https://doi.org/10.5194/esd-13-1397-2022, 2022.

Richardson, D., Black, A. S., Irving, D., Matear, R. J., Monselesan, D. P., Risbey, J. S., Squire, D. T., and Tozer, C. R.: Global increase in wildfire potential from compound fire weather and drought, npj Climate and Atmospheric Science, 5, https://doi.org/10.1038/s41612-022-00248-4, 2022.

Ridder, N. N., Pitman, A. J., Hirsch, A. L., Evans, J. P., Westra, S., Ukkola, A., Hong, X. D., Luca, A. D., Zscheischler, J., and Bador, M.: Global hotspots for the occurrence of compound events, Nature Communications, pp. 1–10, https://doi.org/10.1038/s41467-020-19639-3, 2020.

Rigby, R. A. and Stasinopoulos, D. M.: Generalized Additive Models for Location, Scale and Shape, Journal of the Royal Statistical Society Series C: Applied Statistics, pp. 507–554, https://doi.org/10.1111/j.1467-9876.2005.00510.x, 2005.

Robin, Y., Corre, L., Marson, P., Bernus, S., Vrac, M., and Thao, S.: Projections climatiques régionalisées : correction de biais et changements futurs, Tech. rep., Projet Explore2, https://doi.org/10.57745/KXRB5B, 2024.

Rodrigues, M., Àngel Cunill Camprubí, Balaguer-Romano, R., Coco Megía, C. J., Castañares, F., Ruffault, J., Fernandes, P. M., and Resco de Dios, V.: Drivers and implications of the extreme 2022 wildfire season in Southwest Europe, Science of The Total Environment, 859, https://doi.org/10.1016/j.scitotenv.2022.160320, 2023.

Squire, D. T., Richardson, D., Risbey, J. S., Black, A. S., Kitsios, V., Matear, R. J., Monselesan, D., Moore, T. S., and Tozer, C. R.: Likelihood of unprecedented drought and fire weather during Australia's 2019 megafires, npj Climate and Atmospheric Science, 4, https://doi.org/10.1038/s41612-021-00220-8, 2021.

Stasinopoulos, D. M. and Rigby, R. A.: Generalized Additive Models for Location Scale and Shape (GAMLSS) in R, Journal of Statistical Software, 23, https://doi.org/10.18637/jss.v023.i07, 2007.

Strohmenger, L., Sauquet, E., Bernard, C., Bonneau, J., Branger, F., Bresson, A., Brigode, P., Buzier, R., Delaigue, O., Devers, A., Evin, G., Fournier, M., Hsu, S.-C., Lanini, S., de Lavenne, A., Lemaitre-Basset, T., Magand, C., Mendoza Guimarães, G., Mentha, M., Munier, S., Perrin, C., Podechard, T., Rouchy, L., Sadki, M., Soutif-Bellenger, M., Tilmant, F., Tramblay, Y., Véron, A.-L., Vidal, J.-P., and Thirel, G.: On the visual detection of non-natural records in streamflow time series: challenges and impacts, Hydrology and Earth System Sciences, https://doi.org/10.5194/hess-27-3375-2023, 2023.

Sutanto, S. J., Vitolo, C., Di Napoli, C., D'Andrea, M., and Van Lanen, H. A.: Heatwaves, droughts, and fires: Exploring compound and cascading dry hazards at the pan-European scale, Environment International, 134, https://doi.org/10.1016/j.envint.2019.105276, 2020.

Tipping, M. E. and Bishop, C. M.: Probabilistic Principal Component Analysis, Journal of the Royal Statistical Society: Series B (Statistical Methodology), https://doi.org/10.1111/1467-9868.00196, 1999.

Usman, S., Parker, M., and Vallat, M.: Dry-roasted NUTS: early estimates of the regional impact of 2025 extreme weather, preprint, SSRN, https://doi.org/10.2139/ssrn.5484206, 2025.

Vallet, L., Schwartz, M., Ciais, P., van Wees, D., de Truchis, A., and Mouillot, F.: High-resolution data reveal a surge of biomass loss from temperate and Atlantic pine forests, contextualizing the 2022 fire season distinctiveness in France, Biogeosciences, 20, 3803–3825, https://doi.org/10.5194/bg-20-3803-2023, 2023.

Van Wagner, C.: Development and structure of the canadian forest fire weather index system, Tech. Rep. Forestry Technical Report 35, Canadian Forestry Service, 1987.

Verfaillie, D., Déqué, M., Morin, S., and Lafaysse, M.: The method ADAMONT v1.0 for statistical adjustment of climate projections applicable to energy balance land surface models, Geoscientific Model Development, 10, 4257–4283, https://doi.org/10.5194/gmd-10-4257-2017, 2017.

Vidal, J. P., Martin, E., Franchisteguy, L., Baillon, M., and Soubeyroux, J. M.: A 50-year high-resolution atmospheric reanalysis over France with the Safran system, International Journal of Climatology, 30, https://doi.org/10.1002/Joc.2003, 2010a.

Vidal, J. P., Martin, E., Franchisteguy, L., Habets, F., Soubeyroux, J. M., Blanchard, M., and Baillon, M.: Multilevel and multiscale drought reanalysis over France with the Safran-Isba-Modcou hydrometeorological suite, Hydrology and Earth System Sciences, 14, 2010b.

Wang, J., Chen, Y., and Xia, J.: Anthropogenically-driven increases in the risks of summertime compound hot extremes, Nature Communications, https://doi.org/10.1038/s41467-019-14233-8, 2012.

https://doi.org/10.5194/egusphere-2026-1406
Preprint. Discussion started: 31 March 2026

Zscheischler, J. and Lehner, F.: Attributing Compound Events to Anthropogenic Climate Change, Bulletin of the American Meteorological Society, https://doi.org/10.1175/BAMS-D-21-0116.1, 2022.

Zscheischler, J., Naveau, P., Martius, O., Engelke, S., and Raible, C. C.: Evaluating the dependence structure of compound precipitation and wind speed extremes, Earth System Dynamics, https://doi.org/10.5194/esd-12-1-2021, 2021.